## Soft Matter

## **ARTICLE TYPE**

Cite this: DOI: 00.0000/xxxxxxxxxx

## Phase behaviour of coarse-grained fluids

V. P. Sokhan,\*a M. A. Seaton,a‡ and I. T. Todorova

Received Date

DOI: 00.0000/xxxxxxxxxx

Soft condensed matter structures often challenge us with complex many-body phenomena governed by collective modes spanning wide spatial and temporal domains. In order to successfully tackle such problems mesoscopic coarse-grained (CG) statistical models are being developed, providing a dramatic reduction in computational complexity. CG models provide an intermediate step in the complex statistical framework of linking the thermodynamics of condensed phases with the properties of their constituent atoms and molecules. These allow us to offload part of the problem to the CG model itself and reformulate the remainder in terms of reduced CG phase space. However, such exchange of pawns to chess pieces, or "Hamiltonian renormalization", is a radical step and the thermodynamics of the primary atomic and CG models could be markedly different. Here, we present a comprehensive study of the phase diagram including binodal and interfacial properties of a novel soft CG model, which includes finite-range attraction and supports liquid phases. Although the model is rooted in similar arguments to the Lennard-Jones (LJ) atomic pair potential, its phase behaviour is qualitatively different from that of LJ and features several anomalies such as an unusually broad liquid range, change in concavity of the liquid coexistence branch with variation of the model parameters, volume contraction on fusion, temperature of maximum density in the liquid phase and negative thermal expansion in the solid phase. These results provide new insight into the connection between simple potential models and complex emergent condensed matter phenomena.

### Introduction

Coarse-graining (CG) is now well established as an essential ingredient of multiscale modelling frameworks 1 and provides accelerated pathways to characterizing soft condensed matter<sup>2</sup> including complex fluids<sup>3</sup>, biological membranes<sup>4</sup> and ionic solutions<sup>5</sup>. Despite the inevitable loss in structural detail at the CG level, its enormous potential in expanding the scales drives current advances in complex condensed phases characterization. In order to achieve the desired speedup in soft matter systems both the solutes and solvents need to be coarse-grained consistently. Most forthrightly, CG can be carried out in biological and polymer systems by mapping (macro-)molecular fragments and moieties of chemically connected atomic fragments to "beads" interacting via CG forces <sup>6,7</sup>. Here, CG methods have scored rapid successes from their arrival in the late 1960s, culminating in the 2013 Nobel Prize in Chemistry awarded to Martin Karplus, Michael Levitt and Arieh Warshel "for the development of multiscale models for complex chemical systems"8. Their ideas on simplified protein structures 9 are now broadly adopted in biomolecular simulation and software, e.g., in the Martini force field <sup>10</sup>.

Conversely, CG mapping of solvents, and fluid phases in general, is a less clear-cut problem <sup>11</sup> apparently due to the vague definition of a fluid element in statistical mechanics. Unrestricted motion of atoms in the fluid phase stipulates an open

‡ E-mail: michael.seaton@stfc.ac.uk

system view of CG particles 12 and approaches based on Voronoi tessellation 13,14 and Brownian Quasiparticles 15 have been put forward to tackle this matter, although the problem still remains largely open. Crucially, although CG interactions can be cast in the form of an effective pair potential, the potential is likely to be of a different functional form to that for atomistic systems. Accuracy of CG mapping depends critically on the functional form of the ansatz, which could only be hypothesised. This already poses a problem with bonded interactions, but is a fairly non-trivial problem for non-bonded interactions that involves genuine perception. Existing methods provide the means to optimise the parameters of the model, but not its functional form. Common ansätze validated at the atomic scale, such as the omnipresent Lennard-Jones (LJ) potential, are not necessarily the best candidates for generic effective CG potentials <sup>16</sup>. In fact, the utility of the LJ potential has been recently questioned even at the atomic scale <sup>17</sup>. Furthermore, although it usually goes unquestioned, various bottom-up approaches 18,19 hold the underlying atomic representation as a ground-truth structure. It is important to realise, however, that the atomic data are themselves based on effective empirical pair potentials, likely to be inaccurate away from their training sets.

Another moot point is related to generating adequate representations of many-body interactions using pairwise CG potentials. In general, any adjustment in the Hamiltonian alters the thermodynamic phase behaviour <sup>20</sup>. This is true even if the CG Hamiltonian is obtained using the rigorous Mori-Zwanzig projection operator formalism <sup>21</sup>—the intrinsic reduction in entropy will affect the thermodynamic functions of the CG sys-

a STFC Daresbury Laboratory, Sci-Tech Daresbury, Keckwick Lane, Daresbury, Cheshire WA4 4AD, UK. E-mail: vlad.sokhan@stfc.ac.uk

CG Hamiltonian projection opera

tem<sup>22</sup>. With the reduced set of effective degrees of freedom certain correlations are lost and, with them, all related phenomena can be missed. This problem of representability, which has been often skirted in previous CG studies, is now receiving much attention <sup>22–24</sup>. The development of rigorous bottomup approaches with chemical accuracy is further hampered by the limited transferability of CG models and economic factors, which need to be taken into account: honing the CG model to specific chemistry may require more effort than solving the problem in question at the atomistic level. At the same time, there is always great demand for finding models that would provide greatly simplified points of view, and as such there is a continuous quest for simple generic models with extended representability. Simple intermolecular interactions do not entail simple thermodynamics 25, and analytically simple soft potentials may conceal unexpected macroscopic phenomena <sup>26–28</sup>. In order to shed more light on the impact of CG of a system on its thermodynamics we study the phase diagram of a simple soft pair potential that is a generalization of the standard potential used in Dissipative Particle Dynamics (DPD).

It is well-known that coarse-graining of any set of degrees of freedom results in changes to the governing equations of motion from the Newtonian form to generalised Langevin dynamics (GLE)<sup>21</sup>, i.e., to the dynamics of interacting Brownian particles. Thus, the structure and dynamics of a CG fluid are coupled: a part of the (conservative) interatomic interactions, not captured by the inter-particle interactions at the CG level, is reinstated in the form of non-conservative interactions with the "bath", i.e., in the form of viscous and stochastic forces coupled via the fluctuation-dissipation theorem <sup>29</sup>. We note in passing that, strictly, even atomic-level dynamics are also of the GLE type since empirical interatomic potentials effectively include averaged-out electronic degrees of freedom. While the neglected forces are likely to be insignificant at the atomic level, this is not so at the mesoscopic scale. Incorporating memory effects is a challenging problem and is the focus of current research<sup>30,31</sup>, although no viable scheme for integration of GLE exists as yet. Existing models are usually based on a Markovian (memoryless) approximation, which enormously simplifies the equations of motion but requires effective (mean-field) friction coefficients though obtainable, as has been demonstrated recently 15, by direct ensemble averaging of an atomistic simula-

For large-scale fluid dynamics problems dissipative particle dynamics (DPD)<sup>32</sup> is arguably the most widely used particlebased method describing various aspects of multiphase flow at the mesoscale 11. Being generic, fast and simple to implement, DPD expands the range of accessible time and spatial scales by several orders of magnitude. However, in its standard form the link to a specific chemistry requires a mean-field approximation<sup>32</sup>. Furthermore, DPD employs only repulsive forces to describe the interactions between the beads representing fluid elements. Its phase diagram includes both fluid and solid phases, but misses gas-liquid coexistence. In other words, it is incapable of capturing such liquid interface phenomena as wetting, spreading, and many important capillary effects. A currently adopted way to overcome this serious drawback is to include many-body interactions in the model through an ad-hoc density-dependent term, as is done in many-body DPD (MB-DPD) <sup>33</sup>, with a caveat of thermodynamic inconsistency <sup>34</sup>. Ex-

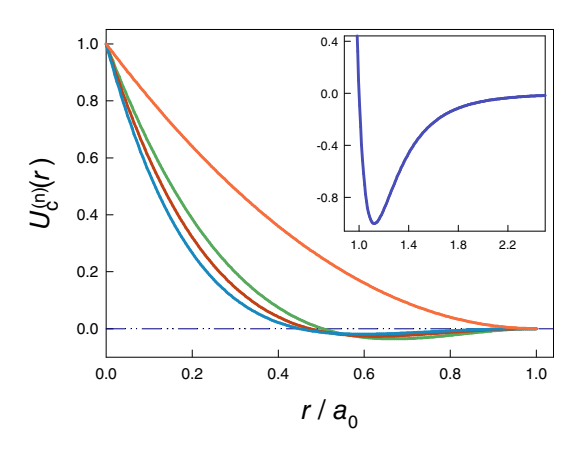


**Fig. 1** Standard DPD (orange line) and new proposed (green, red, and blue lines for n=2, 3, and 4, respectively) showing the attractive region ( $\sim 0.5a_0-1.0a_0$ ). In the inset, the standard Lennard-Jones potential is shown in the reduced units.

plicit many-body terms are not strictly necessary for gas-liquid coexistence, and simple fluid models, which include many-body terms only effectively, capture a wealth of capillary phenomena within the pairwise approximation.

In the van der Waals (vdW) picture of simple liquids, the short-range structure and correlations are defined primarily by inter-particle repulsion, while attraction plays only a minor role<sup>35</sup>. However, both parts actively participate in shaping the phase diagram<sup>36</sup>, which is liable to differ for the CG system as the result of entropy loss. Even for "rigorously" derived CG potentials<sup>23</sup>, isomorphism between atomic and CG phase envelopes is not guaranteed. Attraction is a prerequisite for a stable liquid-gas interface<sup>37</sup>, with different requirements for systems of different dimensionality. Although the relative range of attraction in CG potentials is likely be reduced<sup>27</sup>, it is believed that for 3D systems any finite-range attraction guarantees a first-order liquid-gas transition<sup>38</sup>.

Building on the success of DPD model we extended its conservative interactions to include the attractive term and explore the phase diagram of the new model. The next section of this article outlines the extended potential, termed nDPD, and provides details of simulations. We then present the results of condensed phases simulations using nDPD potentials, demonstrating stable liquid and solid phases for all three studied orders, n = 2, 3, 4. After that we discuss the anomalies in the observed thermodynamic properties and outline our conclusions.

## Simulation methods

#### DPD interactions with attraction

In classical statistical simulations an interaction between spherically-symmetric species is well described by the Mie<sup>39</sup> potential, which in the present notation is written as

$$U^{(n,m)}(r_{ij}) = \left(\frac{n}{n-m}\right) \left(\frac{n}{m}\right)^{\frac{m}{n-m}} \varepsilon \left[ \left(\frac{\sigma}{r_{ij}}\right)^n - \left(\frac{\sigma}{r_{ij}}\right)^m \right], \quad (1)$$

where  $\varepsilon$  and  $\sigma$  are the parameters defining the energy and length scales correspondingly, and n and m (n > m > 3) are the exponents defining together the potential well width and the steepness of the potential at short range. The case n=12, m=6 is the archetypal Lennard-Jones potential  $^6$ , illustrated in the inset to Fig. 1. Although this potential describes accurately a wide range of classical atomistic systems including liquid phases and

the critical phenomena, its use in CG simulations is hindered by several factors. It is too steep at short range <sup>40</sup> and diverges at the origin. Furthermore, as a potential of infinite range, it requires truncation in numerical schemes <sup>17</sup>, and the thermodynamics of a truncated potential are sensitive to the details of truncation <sup>20</sup>. The last two issues have been recently discussed from the atomic perspective <sup>17</sup> but the proposed solution is again aimed at atomistic modelling rather than CG.

Unlike CG potentials for chemically bonded species, which diverge at the origin, coarse-grained non-bonded interactions in complex fluids are likely to be "soft", i.e., bound everywhere 40-42, which is a consequence of intra-particle motion 42,43. Perhaps the most general form of the soft "overlap" potential is the Gaussian potential, which has reappeared in classical statistical studies many times in different guises 16,26,42,44,45. However, its usage has one serious shortcoming: a vanishing force at the origin. A bounded potential is also at the crux of the DPD model - there, the force is at its maximum at the origin, and its softness and continuity enables fast exploration of phase space. A possible way to include both repulsion and attraction in the DPD framework is based on the cubic spline weight functions of smoothed particle hydrodynamics (SPH) 46. Such ad hoc solutions would nevertheless provide little generality and insight, and as with the case of Gaussian potential, would lead to a vanishing force at the origin.

Instead, we put forward a new potential class for CG simulations building on the DPD model as the lowest term in a series expansion, and construct the CG potential by combining two different-order terms: the higher order, n, describing the repulsion and the lower order, m, describing the attraction and taken with the negative sign. We conjecture that by augmenting the DPD potential with a short-ranged attractive part we retain the DPD advantages of accurately describing the collective dynamics of fluid phases, adding the benefit of covering the rich world of capillary phenomena due to integrated positive surface tension. We start from the DPD model, where there are two types of forces between the particles (beads): the conservative (potential) force, which defines the thermodynamic state of the substance (fluid) and the Langevin (dissipative and random) forces, which are responsible for its hydrodynamic behaviour. Here, we focus on the first type,  $\mathbf{F}_{c}(r_{ij})$ , which in the standard DPD model is taken as being linear in the interparticle separation  $r_{ii} \equiv |\mathbf{r_{ii}}|$ ,

$$\mathbf{F}_{c}(r_{ij}) = A_{ij} \left( 1 - \frac{r_{ij}}{r_{c}} \right) \mathbf{e}_{ij}, \tag{2}$$

which arises from the quadratic potential

$$U(r_{ij}) = \frac{1}{2} A_{ij} r_{\rm c} \left( 1 - \frac{r_{ij}}{r_{\rm c}} \right)^2.$$
 (3)

Here,  $\mathbf{e}_{ij} \equiv \mathbf{r}_{ij}/r_{ij}$  is the unit vector in the interparticle direction and  $r_{\rm c}$  is the cutoff distance for interparticle separations beyond which both the force and potential vanish.

Generalizing the conservative force to arbitrary powers n, m,

$$\mathbf{F}_{\mathsf{c}}^{(n,m)}(r_{ij}) = A_{ij} \left[ b_{ij} \left( 1 - \frac{r_{ij}}{r_{\mathsf{c}}} \right)^n - \left( 1 - \frac{r_{ij}}{r_{\mathsf{c}}} \right)^m \right] \frac{\mathbf{r}_{ij}}{r_{ij}}, \quad (4)$$

where the repulsive exponent, n, represents the force order,

**Table 1** Parameters of the nDPD potential in reduced units

n	$A_{ij}$	$b_{ij}$	$\sigma_{\!ij}$
2	25.0	3.02	0.5033
3	15.0	7.2	0.4730
4	10.0	15.0	0.4497

Table 2 Critical Parameters

n	T	p	ρ
2	1.025	0.2951	0.519
3	1.284	0.3979	0.504
4	1.290	0.4095	0.484

which together with the attractive term exponent,  $1 \le m \le n$ , and two other parameters of the model,  $A_{ij}$  and  $b_{ij}$ , completely define the interactions.  $A_{ij}$  is the repulsive parameter with the unit of force, and  $b_{ij}$  is a scaling factor defining the magnitude of repulsion relative to attractive interactions. Here, we consider only the case of m=1, and in the following we omit it completely, denoting the potential as nDPD. The corresponding energy term is, therefore,

$$U_{c}^{(n)}(r_{ij}) = \frac{A_{ij}b_{ij}r_{c}}{n+1} \left(1 - \frac{r_{ij}}{r_{c}}\right)^{n+1} - \frac{A_{ij}r_{c}}{2} \left(1 - \frac{r_{ij}}{r_{c}}\right)^{2}.$$
 (5)

From this expression it is clear that  $b_{ij} > 0.5(n+1)$  is required for  $U_{\rm c}^{(n)}(r_{ij}) = 0$  to have a root  $\sigma$  ( $0 < \sigma < r_{\rm c}$ ). Finally, setting also n=1 and  $b_{ij}=2$  would recover the standard DPD potential.

We considered here only the first three low-order cases, n=2,3,4. They are sketched in Fig. 1, where they are contrasted with the standard DPD potential and LJ potential used in atomistic simulations. With the selected parameters given in Table 1, the location of the first zero of the potential is  $\sim 0.5a_0$ , with a gradual decrease for higher values of n. By contrast, the standard DPD potential decays monotonically to zero at  $a_0$ . A common peculiarity of both DPD and nDPD potentials, distinguishing them from conventional inverse-power ones, is the relationship between the force and the potential exponents: whereas in the former the exponent in the force is lower by one from the potential power, in the latter it is higher by one.

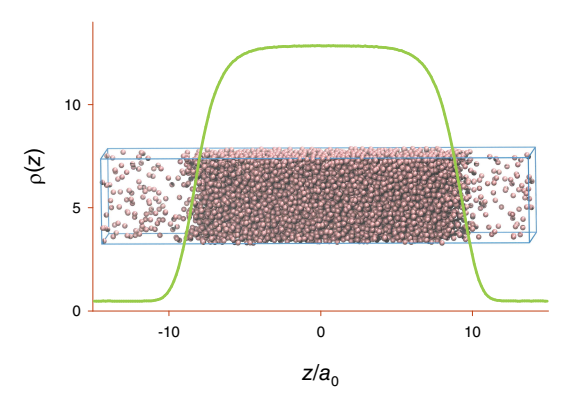


**Fig.** 2 A sketch of the system in slab geometry used to estimate the coexisting densities. The graph presents the density profile of the DPD particles (green line) giving the values of two coexisting densities, where the profile is flat, and showing two liquid-vapour interfaces at  $z\pm 10a_0$ .

#### DPD simulations and units

All DPD calculations were performed using a modified version of the DL\_MESO package  $^{47,48}$  to accommodate the new potential type. We used DPD reduced units  $^6$  throughout, with the following exception: we define the length scale in terms of  $\sigma,$  the shortest distance at which the interparticle potential reaches zero, as is established, e.g., for the LJ potential. We take it as the particle size, as shown in the last column in Table 1. When the properties are expressed in terms of the critical parameters (Table 2), they are denoted by the superscript asterisk.

Integration of the Langevin equations of motion stipulates isothermal conditions. In setting the system and during the *NVT* simulations we used the standard velocity Verlet integrator with the DPD thermostat  $^{48}$ , while for NpT calculations the DPD thermostat and barostat are coupled to Langevin pistons  $^{49}$ .

Since nDPD interactions are of a finite-range, thermodynamic properties require no long-range corrections and the only controllable sources of systematic errors in the results are due to the finite timestep and the system size. Both factors were evaluated and in the simulations we used a dimensionless timestep of 0.005. Due to the finite time step, the system temperature estimated from the ensemble averaged kinetic energy, increases quadratically from the thermostat temperature, typically by 0.1% with the selected timestep. However, by extrapolating to infinitesimal limit the thermostat temperature is recovered. In the fluid part of *n*DPD phase diagram pressure is dominated by the kinetic contribution, and finite time steps lead therefore to a quadratic rise in pressure, amounted to a half percent increase near the critical point. To negate this effect we used the same timestep in all calculations. With regard to the system size, we used between 8000 and 64000 particles depending on the estimated property to make the error due to system size of the order of statistical uncertainty in the results or even smaller.

#### Simulation of orthobaric densities and the solid phase

Coexistence curves were estimated from the series of two-phase calculations performed in slab geometry (see Fig. 2) using rectangular elongated prism-shaped simulation boxes containing between 20000 and 64000 particles. Such a setup allows us to simultaneously estimate both the coexisting pressure and densities at a given temperature, and also the surface tension from the difference in the diagonal pressure components  $^6$ .

Closer to the critical point the coexisting densities can no longer be reliably determined using this setup due to increased fluctuations and spontaneous creation and destruction of interfaces. The coexisting pressure can still, however, be reliably estimated as the normal pressure component along the long axis in a rectangular prism of a high aspect ratio, given that the liquid/gas interfaces have insignificant curvature. This is expected in the proximity of the critical point where the correlation length rapidly grows and the surface tension decreases. We estimated therefore the coexisting densities using a set of isotherms in the subcritical region, as illustrated in Fig. 3. The isotherms were constructed from a set of isochoric calculations of cubic boxes with N=8000 particles of progressively larger sizes. Below the critical temperature they include the van der Waals (wdW) loop as illustrated in the Figure for the T = 1.27and 1.28 cases. Although for finite volumes all states along the isotherms are thermodynamically stable <sup>50</sup>, the regions marked

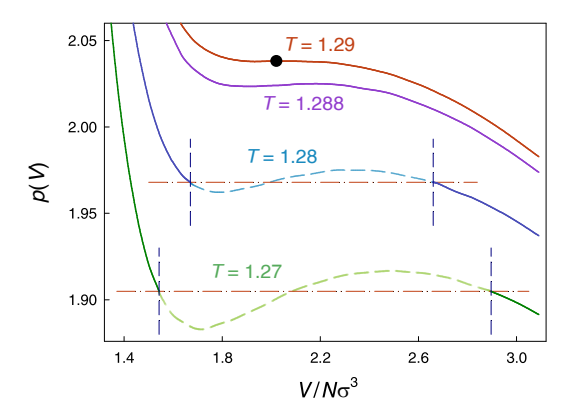


Fig. 3 Pressure as a function of volume per particle in terms of particle size  $\sigma$  for several near-critical isotherms for n=4 potential. Horizontal dash-dotted lines denote coexisting pressure from the two-phase simulation; vertical dashed lines denote the positions of coexisting volumes; black dot marks the critical point. See text for details of estimating the coexisting densities.

by the dashed lines in two lower curves may or may not phase separate inside the boxes  $^{50}$ . These regions, of course, are metastable or completely unstable in the thermodynamic limit, which precludes us from using the Maxwell construction  $^{51}$ . Instead, we used the pressure values obtained in two-phase simulations (the horizontal dashed lines in the Figure) and estimated the coexisting densities from the crossing points with the isotherm where it has a negative slope, as marked by the vertical dashed lines in the Figure. In this way our estimates are based only on thermodynamically safe data from the regions covered by the full lines in the Figure and allowed us to obtain the densities for temperatures as close as  $T=0.99T_{\rm c}$ .

We determined the type of the solid structure by annealing the systems, each containing  $4N^3$  and  $2N^3$  particles (where N is an integer, we used between 12 and 20) and thus promoting formation of BCC and FCC solids correspondingly, and allowing the solid phases to form. We subsequently used common neighbour analysis (CNA), as implemented in the Open Visualization Tool OVITO  $^{52}$ , to analyse the particle trajectories and determine the preferred type of the cubic cell. The ratio of FCC to BCC local structures was more than 20 in all cases, from which we concluded that the equilibrium structure is FCC.

In order to determine the ground state (zero temperature) energy and structure we calculated the energy of the FCC lattice as a function of the nearest-neighbour distance  $r_0$ , the results are shown in Fig. 4. Thermodynamic stability requires the condition that the total configurational energy of a system of N particles is bounded from below  $^{53}$ , i.e., that  $U_N(r^N) \geq -NB$ , where B is a fixed number. The condition is controlled by the potential parameter b, and the values in Table 1 were selected to satisfy it.

The oscillations in energy, well resolved for n=2 potential (Fig. 4, left panel) result from new members of the lattice sum entering the range of potential forces as the system compresses. Their presence indicates the possibility of different polymorphic forms in the solid state, which will be investigated in the future. The inset shows the energy per particle density dependence in the FCC and BCC lattices, indicating a series of FCC $\leftrightarrow$ BCC transitions as the pressure increases.

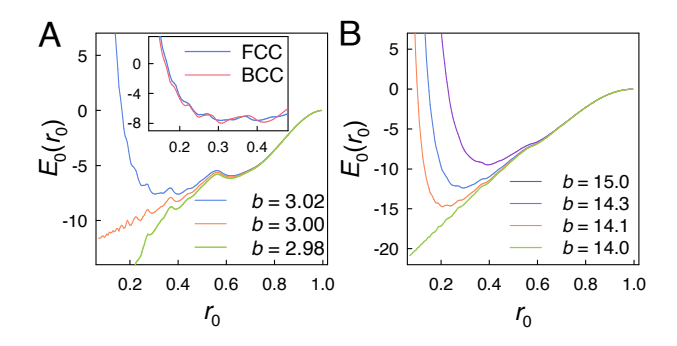


**Fig. 4** Zero-temperature energy per particle as a function of interparticle nearest-neighbour separation. (*A*) FCC lattice with *n*DPD potential n=2 for three values of the repulsion parameter; inset - comparison of FCC and BCC energies for b=3.02. (*B*) energies for n=4 potential for four values of the repulsion parameter.

#### Critical point and critical constants estimation

We determined the location of the critical point from a set of isotherms at progressively increased temperatures. The first isotherm that does not contain the vdW loop, here the T=1.29 isotherm, is deemed to be the critical one. To estimate the critical density of the model we fit the Wegner expansion <sup>54</sup>,  $\rho_{\rm l}(\tau) - \rho_{\rm v}(\tau) = A\tau^{\beta} + B\tau^{\beta+\Delta}$ , where  $\tau = 1 - T/T_{\rm c}$ , to our coexistence data, with  $\beta = 0.32653$  and  $\Delta = 0.5$  assuming the commonly accepted 3D Ising universality class <sup>55</sup> and using the fact that the lattice gas model and the Ising model are isomorphic <sup>56</sup>.

#### Solid-liquid phase transition

In order to locate the solid-liquid transition control parameters (transition temperature in the T-scan and transition pressure for pressure-induced melting) we initially established the approximate area of transition by scanning the control parameters and monitoring the density (volume) for a system of N = 32000particles. This gave us roughly  $\pm 20\%$  margins in the control parameters around the transition. To solve the nucleation problem, we then prepared an initial two-phase state by equilibrating separately bulk liquid and bulk solid samples using the parameters outside of the transition margins and then bringing the two systems in contact, watching for the absence of significant overlaps at the flat boundary. Using a sample of N = 64000particles with one half in a typical liquid configuration and the other in a typical solid one, we conducted a series of short NpTsimulations at progressively higher values of the control parameter, monitoring the kinetics of the interphase boundary. The direction of the boundary motion (towards freezing or melting of the whole sample) appears to be a sensitive indicator of the ensuing phase, insensible to the initial configurations, and we were able to locate the transition within a  $\pm 1\%$  margin for the temperature and within  $\pm 10\%$  for the pressure.

#### Results

#### Properties along the liquid-gas coexistence curve

Using the *n*DPD potential with n = 2,3,4, we explored both branches of the binodal of their fluid phases from the triple point to the critical point. The binodal curves presented in Fig. 5 in reduced units (with respect to the corresponding critical density and critical temperature, see Table 2) demonstrate several unusual features. First, the liquid phase in the *n*DPD model has a much wider extent than simple atomic liquids and

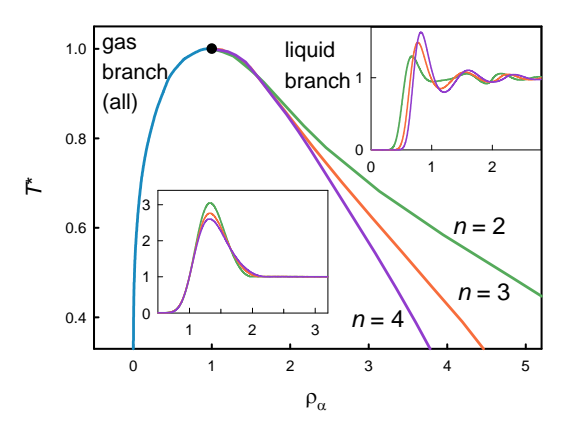


**Fig.** 5 Coexistence curves for the new potential, calculated for quadratic, cubic, and quartic repulsive forces at certain values of parameters. The blue line denotes the gas branch (common for all powers) and the green, orange, and red lines are for the liquid branches. The black dot denotes the critical point. Reduced units have been used with critical values defining the scales. (*Insets*) Radial distribution functions at the coexistence densities: left - gas branch, right - liquid branch, at  $T^* = 0.4$  for the three potential classes.

water. For example, the freezing transition at zero pressure for the n=4 (4DPD) potential occurs at  $T^*=0.0709$  (T=0.0915), whereas argon has the triple point at  $T^*=0.556$ , and water at  $T^*=0.422$ . Second, while the gas branch in all three cases falls on the same curve on the scale of the figure, the liquid branches are markedly different outside of the scaling region. Even the concavity of the liquid branch varies with the parameter b of the potential: with the selected parameters the liquid branch is concave for n=4, a straight line for n=3, and a convex curve for n=2, challenging the law of corresponding states. We have verified that the n=2 branch becomes concave when b increases from 3.02 to 3.1. The straight line appears to be the limiting case for  $n \geq 3$  (See *Methods*). In the scaling region near the critical point all liquid branches collapse onto a single universal curve.

The insets to the Figure illustrate the radial distribution functions (RDF) for both branches at a representative temperature. For the gas branch all cases display a typical low-density atomic (e.g., LJ fluid) RDF, with its height increasing with the potential well depth: more so for lower powers of potential (n). Conversely, the liquid RDFs show a transition from the usual simple fluid liquid-density RDFs for the two higher powers to an unusual fluid for the 2DPD potential with the second minimum more pronounced than the first, where the positions of the first and the third solvation shells are also shifted to shorter distances but the position of the second one remains unchanged.

We calculated the surface tension  $\gamma$  as a function of temperature and, by fitting the data to a power law  $\gamma \propto (T_{\rm C}-T)^{\mu}$ , we obtained an independent estimate of the critical temperature. For the 4DPD potential, illustrated in Fig. 6A,  $T_{\rm C}=1.28(2)$ , in excellent accordance with the value obtained from the binodal data ( $T_{\rm C}=1.29$ ). The second parameter of the fit, the critical exponent  $\mu$ , has a converged value of 1.38, deviating somewhat from the accepted value for fluids,  $\mu=1.28(6)^{57}$ . In the Figure we expressed the surface tension in the standard DPD units (length in units of potential range a). This facilitates the comparison with experimental data for key solvents. For example, water modelled as a DPD fluid, with an a=8.52 Å (7:1) mapping would have a surface tension of  $\gamma=12.7$  at  $T^*=0.46$ 

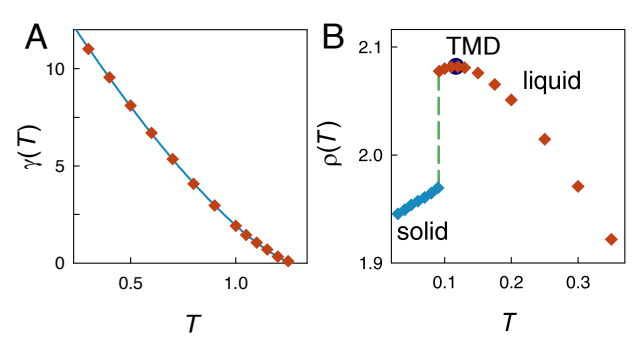


Fig. 6 (A) Calculated surface tension of 4DPD liquid in DPD units as a function of temperature up to the critical point. Solid line is a power law fit (see text). (B) Temperature dependence of density around the solid-liquid phase transition. Red diamonds - liquid phase, blue diamonds - solid phase, and the temperature of transition is marked by the green dashed line. The large blue dot indicate the position of the temperature of maximum density (TMD).

(based on 72.0 mN m<sup>-1</sup> at  $T = 298 \text{ K}^{58}$ ).

# Contraction on fusion, temperature of maximum density, and negative thermal expansion in the solid

At low temperatures, an nDPD fluid freezes for all three studied classes, which is where it exposes another unusual behaviour. Whereas most substances expand when heated, there is a compelling group of materials that contract upon heating within a certain temperature range. Classic textbook examples include liquid water below 4 °C (277 K) and ice below 63 K<sup>59</sup>. This phenomenon, termed Negative Thermal Expansion (NTE)60, occurs when materials contract in volume upon heating and is characterised by the negative value of the bulk thermal expansion coefficient,  $\alpha = (\partial \ln V / \partial T)_p < 0$ . NTE in complex materials with directional bonding, where it is more often found <sup>60,61</sup>, received much attention in recent years due to its industrial applications. Molecular mechanisms explaining NTE in these systems include, inter alia, Grüneisen vibrational theory of thermal expansion <sup>60,62</sup>, special phonon properties <sup>61</sup>, and rigid unit modes <sup>61</sup>. At the same time, there are a few pure elements where the NTE and contraction of fusion have been found, which cannot be explained by the above mechanisms. These elements include semimetal bismuth, the metals gallium and plutonium, and the metalloids antimony, germanium, and silicon. They crystallise into different crystal structures <sup>63</sup>, belong to different groups in the periodic table, and exhibit markedly different NTE ranges: it is thus unlikely that their behaviour can be attributed to unique electronic properties alone. There is no clear understanding of the underlying mechanisms in these systems. Furthermore, several classical single-component model systems with isotropic pair potentials, such as the purely repulsive Gaussian core model<sup>26,64</sup>, as well as the ad hoc devised potentials with a softened interior of their basins of attraction 65, also feature NTE. However, finding a simple model with an isotropic potential, which reproduces the anomalous behaviour of water—contraction on melting with an immediate negative expansion region in the liquid phase—is known to be a challenging open problem 65. Here, we demonstrate that the nDPD model includes all of the essential ingredients required to capture this complex phenomenon.

In order to locate the solid-liquid phase transition we calculated the isobaric density of nDPD at low temperatures. The

results for the n=4 potential at zero external pressure are presented in Fig. 6B. The freezing transition occurs at T=0.0729 ( $T^*=0.0760$ ) for the 2DPD potential, at T=0.0873 ( $T^*=0.0680$ ) for the 3DPD potential, and at T=0.0915 ( $T^*=0.0709$ ) for the 4DPD potential. The system freezes into an FCC solid with an expansion in volume of ca 5.5% in all three cases. Just before freezing a density maximum is observed at T=0.11 ( $T^*=0.0852$ ) for the 4DPD case. On the liquid side, it qualitatively describes water, which has a temperature of maximum density (TMD) of 4 °C (277 K) or, in reduced units,  $T^*\approx 0.4283$ . Even taking into account that water expands by 9% upon freezing, nDPD presents alternatives to hydrogen bonding mechanisms that lead to the qualitatively same effect, which could be explored further when developing accurate CG water models.

#### Pressure-induced melting

If the liquid phase of a substance is more dense than its solid phase, the melting temperature decreases with increased pressure. This general result, which follows from the Clausius-Clapeyron equation, is well known for water, where a regelation occurs for up to 20 K below the normal freezing point. A similar phenomenon is also observed for the chemical elements mentioned in the previous section that feature NTE, as well as in alkali metals. Using the two-phase setup to study the solidliquid transitions, we observed a monotonous decrease in transition temperature from  $T^* = 0.0709$  at effectively zero pressure down to  $T^* \approx 0.03$  at p = 10 for a 4DPD potential. As a consequence of this, there is a maximum temperature for which the solid phase exists for the *n*DPD model:  $T^* = 0.0709$  for 4DPD. For temperatures below this maximum value, the system melts when pressurised. It should be noted that other models feature pressure-induced melting. For example, in the Gaussian core model<sup>26</sup> reentrant melting has been reported<sup>66</sup>.

## **Discussion and Conclusions**

In his milestone paper discussing the hierarchical structure of science, "More is different", Phillip Anderson argued that behaviour of complex systems cannot be entirely "understood in terms of a simple extrapolation of the properties of a few particles", and that "at each level of complexity entirely new properties appear" <sup>67</sup>. As we dial down the magnification moving to larger scales, we would find the new phenomena in focus, and these phenomena might or might not be present at finer resolutions. Coarse-graining is a powerful tool for dealing with complex (macro-)molecular systems, where molecular fragments or even entire molecules are replaced with individual CG sites. However, when it comes to non-bonded interactions, even key questions such as bottom-up derivation of the CG fluid particle potential and sensible criteria for the scaling factor remain open <sup>11,15</sup>.

Despite the wide popularity of the DPD model <sup>11</sup>, little justification has been provided for its linear conservative force <sup>32</sup>. It might therefore be surprising that a simple repulsive force of the DPD model can provide a working solution for many cases <sup>11</sup>. To qualitatively understand this success, imagine a coarse-graining process with progressively larger scaling factors. The liquid structure is defined in terms of density correlations, which includes—according to the Ornstein-Zernike (OZ) approach <sup>68</sup>—a short-ranged component referred to as a direct

correlation function. In the OZ picture the total correlation between two particles is composed of the direct correlation and an indirect part, which is longer-ranged and composed of all possible particle chains of direct correlation in the fluid <sup>68</sup>. In the CG process the direct correlations are averaged out, which leaves just indirect correlations to be reproduced by a suitable ansatz. At this level of CG the interactions are much softer, and we argue that they are captured by the *n*DPD model. Since much of the chemical specificity is absorbed within the short range, the longer-range correlations are of a more generic nature. At even higher CG scaling most of the correlation is averaged out, leaving only the soft elastic repulsion between the beads due to the finite compressibility of the fluid. The interactions emerging at this scale are therefore of the DPD type.

As we have demonstrated, the nDPD potential with appropriate choices for its three parameters is able to produce stable liquid and solid phases. At the same time, the phase diagram of *n*DPD matter is topologically different from that of simple atomic systems, with the solid phase occupying a narrow density region at low temperatures. The thermodynamics of its condensed phases is rich with anomalous features, usually attributed to complex molecular systems. They include expansion on freezing, temperature of maximum density, negative thermal expansion in the solid phase, an unusual liquid-vapour phase envelope and pressure-induced melting. In this work, we have not explored in full the model parameter space, particularly the relative range of the attraction, which is likely to conceal additional anomalies. However, the fact that the anomalies are found in systems with soft coarse-grained isotropic pair potentials indicates that they likely to originate in the mediumrange structure, i.e., beyond the first neighbours in the underlying atomistic system. The complex phase behaviours have also been found in models with coarse-grained bonded interactions <sup>25,27</sup> and were observed in colloidal suspensions <sup>69</sup>.

Clearly, no CG model can reproduce the whole spectrum of observables of the underlying atomistic model, in the same way as no atomistic model can reproduce the entire set of experimental observables. This is a manifestation of the representability problem<sup>24</sup>, which arises due to the resolution change at the mean-field level: certain correlations are missing. Thus, a CG model cannot describe the processes of self-assembly or gelation, which involve changes in fine-level molecular topology. However, this is not the purpose of the model. Rather, each model level in the hierarchy defines its own classes of *compatible* observables that reproduce the experimental observables within the model constraints<sup>24</sup>. A good model goes beyond this and has predictive power. Paraphrasing the famous designer Yves Saint-Laurent, one can say that a good model can advance the field by ten years<sup>70</sup>.

#### Conflicts of interest

There are no conflicts to declare.

#### Acknowledgements

This work was supported by the UKRI's Innovation and Development Programme (IDP) and made use of computational support by CoSeC, the Computational Science Centre for Research Communities, through the High-End Computing Materials Chemistry Consortium (MCC).

#### Notes and references

- 1 W. Noid, G. S. Ayton, S. Izvekov and G. A. Voth, *Coarse-graining of condensed phase and biomolecular systems*, CRC press, Boca Raton, 2008, pp. 21–40.
- 2 S. R. Nagel, Rev. Mod. Phys., 2017, 89, 025002.
- 3 C. Peter and K. Kremer, Soft Matter, 2009, 5, 4357-4366.
- 4 M. Sadeghi and F. Noé, Nat. Commun., 2020, 11, 2951.
- 5 L. I. Vazquez-Salazar, M. Selle, A. H. de Vries, S. J. Marrink and P. C. T. Souza, *Green Chem.*, 2020, **22**, 7376–7386.
- 6 M. P. Allen and D. J. Tildesley, *Computer simulation of liquids*, Oxford: Oxford University Press, 2017.
- 7 M. G. Saunders and G. A. Voth, *Annu. Rev. Biophys.*, 2013, 42, 73–93.
- 8 M. Karplus, Angew. Chem. Int. Ed., 2014, 53, 9992–10005.
- 9 M. Levitt and A. Warshel, Nature, 1975, 253, 694-698.
- 10 P. C. T. Souza, R. Alessandri, J. Barnoud, S. Thallmair, I. Faustino, F. Grünewald, I. Patmanidis, H. Abdizadeh, B. M. H. Bruininks, T. A. Wassenaar, P. C. Kroon, J. Melcr, V. Nieto, V. Corradi, H. M. Khan, J. Domański, M. Javanainen, H. Martinez-Seara, N. Reuter, R. B. Best, I. Vattulainen, L. Monticelli, X. Periole, D. P. Tieleman, A. H. de Vries and S. J. Marrink, Nat. Methods, 2021, 18, 382–388.
- 11 P. Español and P. B. Warren, J. Chem. Phys., 2017, 146, 150901.
- 12 G. Ciccotti and L. Delle Site, *Soft Matter*, 2019, **15**, 2114–2124
- 13 M. Serrano and P. Español, Phys. Rev. E, 2001, 64, 046115.
- 14 E. G. Flekkøy and P. V. Coveney, *Phys. Rev. Lett.*, 1999, **83**, 1775–1778.
- 15 V. P. Sokhan and I. T. Todorov, *Mol. Simul.*, 2021, **47**, 248–256.
- 16 B. J. Berne and P. Pechukas, J. Chem. Phys., 1972, 56, 4213–4216.
- 17 X. Wang, S. Ramírez-Hinestrosa, J. Dobnikar and D. Frenkel, *Phys. Chem. Chem. Phys.*, 2020, **22**, 10624–10633.
- 18 S. Izvekov and G. A. Voth, *J. Phys. Chem. B*, 2005, **109**, 2469–2473.
- 19 M. S. Shell, J. Chem. Phys., 2008, 129, 144108.
- 20 T. Coussaert and M. Baus, Phys. Rev. E, 1995, 52, 862-869.
- 21 R. Zwanzig, *Nonequilibrium statistical mechanics*, Oxford: Oxford University Press, 2001.
- 22 N. J. H. Dunn, T. T. Foley and W. G. Noid, *Acc. Chem. Res.*, 2016, **49**, 2832–2840.
- 23 W. G. Noid, J. Chem. Phys., 2013, 139, 090901.
- 24 J. W. Wagner, J. F. Dama, A. E. P. Durumeric and G. A. Voth, *J. Chem. Phys.*, 2016, **145**, 044108.
- 25 G. Malescio, J. Phys. Condens. Matter, 2007, 19, 073101.
- 26 F. H. Stillinger, J. Chem. Phys., 1976, 65, 3968-3974.
- 27 C. F. Tejero, A. Daanoun, H. N. W. Lekkerkerker and M. Baus, *Phys. Rev. Lett.*, 1994, **73**, 752–755.
- 28 S. Prestipino, C. Speranza, G. Malescio and P. V. Giaquinta, *J. Chem. Phys.*, 2014, **140**, 084906.
- 29 N. G. Van Kampen, *Stochastic processes in physics and chemistry*, Elsevier, Amsterdam, The Netherlands, 2007.

- 30 C. Hijón, P. Español, E. Vanden-Eijnden and R. Delgado-Buscalioni, *Faraday Discuss.*, 2010, **144**, 301–322.
- 31 V. Klippenstein, M. Tripathy, G. Jung, F. Schmid and N. F. A. van der Vegt, *J. Phys. Chem. B*, 2021, **125**, 4931–4954.
- 32 R. D. Groot and P. B. Warren, *J. Chem. Phys.*, 1997, **107**, 4423–4435.
- 33 P. B. Warren, Phys. Rev. E, 2003, 68, 066702.
- 34 A. A. Louis, J. Phys. Condens. Matter, 2002, 14, 9187-9206.
- 35 J. D. Weeks, D. Chandler and H. C. Andersen, *J. Chem. Phys.*, 1971, **54**, 5237–5247.
- 36 B. Smit and D. Frenkel, *J. Chem. Phys.*, 1991, **94**, 5663–5668.
- 37 P. C. Hemmer and J. L. Lebowitz, *Phase transitions and critical phenomena*, London: Academic Press, 1976, vol. 5b, pp. 107–203.
- 38 P. C. Hemmer and G. Stell, *Phys. Rev. Lett.*, 1970, **24**, 1284–1287.
- 39 G. Mie, Ann. Phys., 1903, 316, 657-697.
- 40 C. N. Likos, Phys. Rep., 2001, 348, 267-439.
- 41 J.-P. Hansen and H. Löwen, *Bridging Time Scales: Molecular Simulations for the Next Decade*, Berlin: Springer-Verlag, 2002, pp. 167–196.
- 42 C. N. Likos, H. Löwen, M. Watzlawek, B. Abbas, O. Jucknischke, J. Allgaier and D. Richter, *Phys. Rev. Lett.*, 1998, **80**, 4450–4453.
- 43 S. H. L. Klapp, D. J. Diestler and M. Schoen, *J. Phys. Condens. Matter*, 2004, **16**, 7331–7352.
- 44 P. J. Flory and W. R. Krigbaum, *J. Chem. Phys.*, 1950, **18**, 1086–1094.
- 45 J. A. Purton and W. Smith, Mol. Simul., 2010, 36, 796-800.
- 46 M. Liu, P. Meakin and H. Huang, *Phys. Fluids*, 2006, **18**, 017101.
- 47 M. A. Seaton, R. L. Anderson, S. Metz and W. Smith, *Mol. Simul.*, 2013, **39**, 796–821.
- 48 M. A. Seaton, Mol. Simul., 2021, 47, 228-247.
- 49 A. F. Jakobsen, J. Chem. Phys., 2005, 122, 124901.

- 50 K. Binder, B. J. Block, P. Virnau and A. Tröster, *Am. J. Phys.*, 2012, **80**, 1099–1109.
- 51 J. C. Maxwell, Nature, 1875, 11, 374-377.
- 52 A. Stukowski, Model. Simul. Mat. Sci. Eng., 2009, 18, 015012.
- 53 M. E. Fisher and D. Ruelle, *J. Math. Phys.*, 1966, 7, 260–270.
- 54 F. J. Wegner, Phys. Rev. B, 1972, 5, 4529-4536.
- 55 F. J. Wegner, *Phase transitions and critical phenomena*, NY: Academic Press, 1976, vol. 6, pp. 7–124.
- 56 T. D. Lee and C. N. Yang, Phys. Rev., 1952, 87, 410-419.
- 57 B. Widom, *Phase transitions and critical phenomena*, NY: Academic Press, 1976, vol. 2, pp. 79–100.
- 58 N. R. Pallas and Y. Harrison, *Colloids Surf.*, 1990, **43**, 169–194.
- 59 G. Dantl, Z. Physik, 1962, 166, 115-118.
- 60 M. T. Dove and H. Fang, Rep. Prog. Phys., 2016, 79, 066503.
- 61 A. K. A. Pryde, K. D. Hammonds, M. T. Dove, V. Heine, J. D. Gale and M. C. Warren, J. Phys. Condens. Matter, 1996, 8, 10973–10982.
- 62 G. D. Barrera, J. A. O. Bruno, T. H. K. Barron and N. L. Allan, *J. Phys. Condens. Matter*, 2005, **17**, R217–R252.
- 63 D. A. Young, *Phase diagrams of the elements*, Berkeley: Univ of California Press, 1991.
- 64 F. H. Stillinger and D. K. Stillinger, *Phys. A: Stat. Mech. Appl.*, 1997, **244**, 358–369.
- 65 M. C. Rechtsman, F. H. Stillinger and S. Torquato, *J. Phys. Chem. A*, 2007, **111**, 12816–12821.
- 66 P. V. Giaquinta and F. Saija, ChemPhysChem, 2005, 6, 1768– 1771.
- 67 P. W. Anderson, Science, 1972, 177, 393–396.
- 68 J. S. Rowlinson and F. L. Swinton, *Liquids and Liquid Mixtures*, Butterworths, London, 1982.
- 69 P. N. Pusey and W. van Megen, *Nature*, 1986, **320**, 340–342.
- 70 Ritz Newspaper, 1984.